International Journal of Heat and Mass Transfer 54 (2011) 2043–2055

Contents lists available at ScienceDirect

International Journal of Heat and Mass Transfer

journal homepage: www.elsevier.com/locate/ijhmt

Numerical analysis of microwave melting of ice-saturated porous medium filled in a rectangular waveguide with resonator using a combined transfinite interpolation and PDE methods

Khomgris Chaiyo, Phadungsak Rattanadecho *

Research Center of Microwave Utilization in Engineering (R.C.M.E.), Department of Mechanical Engineering, Faculty of Engineering, Thammasat University (Rangsit Campus), Pathumthani 12120, Thailand

ARTICLE INFO

Article history:
Received 23 March 2010
Received in revised form 3 December 2010
Accepted 3 December 2010
Available online 27 January 2011

Keywords:
Microwave
Melting
Transfinite interpolation
PDE mapping
Moving boundary
Resonator

ABSTRACT

A numerical study is performed for the melting process of ice-saturated porous medium filled in a rectangular waveguide with a resonator subjected to electromagnetic energy. A microwave system supplies a monochromatic wave in a fundamental mode (TE_{10} mode) with operating frequency of 2.45 GHz. Focus is placed on establishing a computationally efficient approach for solving moving boundary heat transfer problem in a two-dimensional structured grid. Numerically, preliminary grids are first generated by an algebraic method, based on a transfinite interpolation method, with subsequent refinement using a PDE mapping method. A preliminary case study indicates successful implementation of the numerical procedure. The predicted results from two-dimensional melting model are then validated against available experimental results and subsequently used as a tool for efficient computational prototyping. Based on the numerical results are performed illustrating the influence of resonator and layered configuration, in case of the installed resonator has strongly affected on the microwave power absorbed, temperature distribution, and the melting front during microwave melting process.

1. Introduction

The study of melting process in material exposed to microwave has been investigated by many researchers. Pangrle et al. [1] studied coupled electromagnetic and thermal model for the thawing process of frozen cylinders (water and NaCl) using a plane wave as opposed to a resonant cavity. They also developed a one-dimensional model for microwave thawing of cylindrical samples [2]. Rattanadecho [3] recently presented theoretical and experimental investigation of microwave thawing of frozen layer in a microwave oven using coordinate transformation technique based on boundary fixed grid method together with an implicit time scheme. A number of other analyses of the microwave thawing process have appeared in the literatures [4,5]. Moreover, most previous work the microwave power absorbed term was assumed to be decay exponentially into the sample following Lambert's law. This assumption is only valid for the large dimension samples where the depth of sample is much larger than the penetration depth. Otherwise in the thin samples where the depth of sample is much smaller than the penetration depth, the spatial variations of the electromagnetic field and microwave power absorbed within sample must be obtained by Maxwell's equation. The prior investigation of two-dimensional microwave melting in cylinders was carried out by Zeng and Faghri [6], and their model predictions were compared with experimental data. Basak and Ayappa [7] also considered the two-dimensional microwave thawing studies with fixed grid based effective heat capacity method coupled with Maxwell's equations. The primary focus of their article is to incorporate and investigate the effect of liquid convection during thawing of a pure material with microwave. For previous work numerically results were performed using the conventional methods such as finite difference and finite element method.

In addition, Rattanadecho [8] developed two-dimensional models to predict the electromagnetic fields (TE_{10} mode) inside the waveguide, microwave power absorbed, and temperature distributions within wood located in rectangular waveguide. In this study, the simulation results were shown to influence of irradiation time, working frequency and sample size on heating patterns were investigated in details. Rattanadecho and Klinbun [9] then recently carried out theoretically analysis of microwave heating of dielectric materials with various resonator distances. This study found that the resonator was significantly affected on a uniformity of temperature distributions depending on the penetration depth of microwave. Furthermore, Rattanadecho et al. [10] investigated numerically and experimentally the melting of frozen packed beds by a microwave with a rectangular waveguide in case of without installed resonator. However, the studied in case of microwave

* Corresponding author. Tel.: +66 2564 3001 9x3153; fax: +66 2564 3010.
E-mail address: ratphadu@engr.tu.ac.th (P. Rattanadecho).

0017-9310/$ - see front matter © 2011 Elsevier Ltd. All rights reserved.
doi:10.1016/j.ijheatmasstransfer.2010.12.024

Nomenclature

a	thermal diffusivity (m^2/s)
A, B	univariate blending function (−)
C_p	specific heat capacity (J/(kg K))
E	electric fields intensity (V/m)
f	frequency of incident wave (Hz), and interpolation function (−)
H	magnetic field intensity (A/m)
L	latent heat (J/kg)
P	power (W)
Q	local electromagnetic energy term (MW/m^3)
S	Poynting vector (W/m^2)
T	temperature (°C)
t	time (s)
$\tan\delta$	dielectric loss coefficient (−)
u, w	interpolation parameter (−)
x, z	Cartesian coordinates
Z_H	wave impedance (Ω)
Z_I	intrinsic impedance (Ω)

Greek letters

ε	permittivity (F/m)
λ	thermal conductivity (W/m K), and wavelength (m)
μ	magnetic permeability (H/m)
υ	velocity of propagation (m/s)
ρ	density (kg/m^3)
σ	electric conductivity (S/m)
ξ, η	transformed coordinates

Subscripts

in	input
l	unfrozen
mov	moving boundary
s	frozen

melting of ice-saturated porous medium including resonator effects has not been investigated before.

Transient heat transfer problem involving melting or solidification processes generally refer to as moving boundary or phase change problems. They are important topics which span a broad spectrum of scientific and engineering discipline such as thawing of freezing of soil, ice formation, food processing and numerous others. The some up to date reviews of these problems are available [11,12]. In the past, a variety of conventional numerical techniques have been developed for solving these problems, including the enthalpy [13,14], isotherm migration [15], and coordinate transformation methods [16,3]. Previous works on multidimensional moving boundary problems include Chatterjee and Prasad [17] adopted a generalized finite volume discretization scheme using a nonorthogonal curvilinear body-fitted transformation, which inherently facilitates accurated tracking of moving interfaces via adaptive grid generation in a full 3D framework, and Gong and Mujumdar [18] used the streamline Upwind/Petrov Galerkin finite element method in combination with fixed grid primitive variable method to simulate melting of a pure phase change material in 2D rectangular container.

Conventionally numerical methods have been widely used due to easy to handle numerical algorithms for phase change problem. However, in numerical approximations used in this method with discontinuous coefficients, often the largest numerical errors are introduced in a neighborhood of the discontinuities particularly for phase change in geometry complexity as well as boundary condition.

The troublesome numerical errors in conventional method are effectively reduced if the grid generation and solution procedure are separated with the discontinuities and special formulas are used to incorporate the jump conditions directly into the numerical model. This is the main idea behind this work considering moving boundary as a parameter.

To create a computational grid in body-fitted coordinates, two basic steps required: (1) define an origin point and (2) specify the distribution (number and spacing) of grid nodes along the edges of the geometric regions. The automatic grid generator then takes over, and using an algebraic technique known as transfinite interpolation, creates a grid that simultaneously matches the edge node prescription and conforms to the irregular edges of the body-fitted geometry. Grid generation by algebraic methods produces high quality numerical grids and allow for the very efficient integration of the thermal-flow field physics. Considering grid optimization, the designed grid optimization-algorithm improves upon the transfinite interpolation method by carrying the grid generation process one step further. It uses automatically generated grid as an initial approximation to a higher quality grid system derived utilizing the technique of PDE grid generation. This technique offers advantages over purely algebraic methods:

- Good control over the skewness and spacing of the derived grid on surface interiors, while simultaneously allowing complete control over the grid spacing (node distribution) on surface edges as well as moving boundary.
- An ability to produce unique, stable, and smooth grid distributions free of interior maxima or minima (inflection points) in body-fitted coordinates.

Parabolic grid generation works well with irregularly shaped geometries and can produce grids that are highly conformal with the edges of individual computational surfaces. The means for grid generation should not be dictated by the limitations of a given specific field solution procedure and conversely the method that determines the field should accept as input an arbitrary set of coordinate points which constitutes the grid. In general, of course, these two operations can never be totally independent because the logistic structure of the information, the location of outer boundaries, the nature of coordinate and the types of grid singularities are items that have to be coordinated closely between the field solver and the grid generator [19].

Grid generation for multi-dimensional geometries using transfinite interpolation functions was studied by Cook [20], Gordon and Hall [21], Ettouney and Brown [22] successfully modeled slightly non-planar interfaces by using an algebraic grid generation system where the interface was described in terms of univariate function.

Although grid generation is the heart of most numerical algorithms for flow problems or non-phase change problem, little effort has been reported on phase change problems, particularly the problem that is to couple the grid generation algorithm with the heat transport equations.

The present paper introduces the novel numerical approach, a combined transfinite interpolation and PDE methods [23,24], for solving two-dimensional melting model under electromagnetic energy which is subjected to a monochromatic microwave TE_{10} mode with operating frequency of 2.45 GHz. However, the effect of resonator on microwave phenomena in the case of using a rectangular waveguide with a resonator has not been clearly studied yet. The

objective of this study can be summarized as follows: (i) It is carried out to predict the melting front, the distribution of temperatures, microwave power absorbed terms, and electromagnetic fields and (ii) The influences of resonator and layered configurations on melting process are clarified in details. Furthermore, numerically in order to generate a boundary/interface fitted coordinate system, structured grids are initialized using transfinite interpolation algebraic techniques and the quality of structured grids can be significantly improved by applying parabolic-PDE methods. These methods iteratively solve unsteady conduction's equation together with moving boundary condition during the melting process considering conduction as the only mode of heat transfer in both the unfrozen layer and the frozen layer.

2. Experimental configuration

Fig. 1 shows the experimental apparatus for microwave melting system. It was developed for the melting tests to validate the model simulation. The rectangular waveguide system is operated by propagating traveling waves along the z-direction of the rectangular waveguide with the inner dimensions of 109.2×54.6 mm toward a water load that is situated at the end of the waveguide. The water load (lower absorbing boundary) ensures that only a minimal amount of microwave is reflected back to the sample. Also, an isolator (upper absorbing boundary), which is located at the upper end of waveguide, is used to trap any microwave reflected from the sample to prevent it from damaging the magnetron. In the microwave supply system a magnetron generated the monochromatic wave of TE_{10} mode with operating frequency of 2.45 GHz, and output of magnetron is adjusted as 1000 W [8].

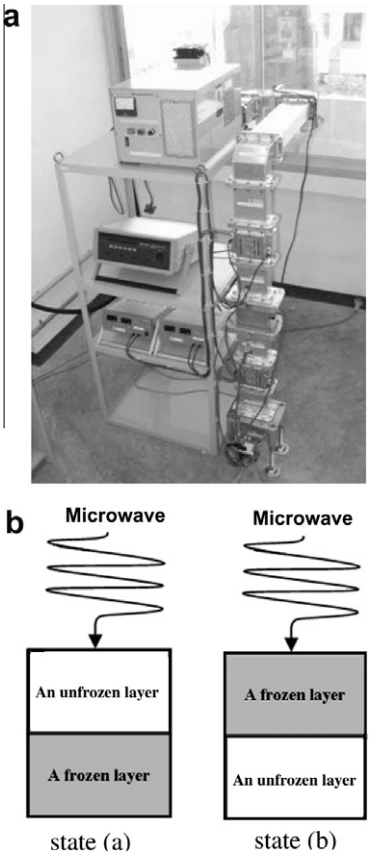

Fig. 1. Experimental apparatus: (a) microwave heating system and (b) the melting sample.

Table 1
Thermal and dielectric property of the unfrozen and frozen layer.

Properties	Unfrozen layer	Frozen layer
ρ (kg/m^3)	1942.0	1910.0
a (m^2/s)	0.210×10^{-6}	0.605×10^{-6}
λ (W/m K)	0.855	1.480
C_p (J/kg K)	2.099×10^3	1.281×10^3
μ_r (−)	1.0	1.0
ε_r (F/m)	$88.15 - 0.414T + (0.131 \times 10^{-2})T^2 - (0.046 \times 10^{-4})T^3$	5.1
$\tan\delta$ (−)	$0.323 - (9.499 \times 10^{-3})T + (1.27 \times 10^{-4})T^2 - (6.13 \times 10^{-7})T^3$	0.0124

Next, the samples used for testing in microwave melting processes are considered. The sample is composed of an unfrozen layer (water and glass beads) with thickness of 50 mm and a frozen layer (ice and glass beads) with thickness of 50 mm. They are arranged in series against perpendicular to direction of irradiation via a rectangular waveguide. The unfrozen layer and the frozen layer are arranged in different configurations, as shown in state (a) and state (b) of Fig. 1(b), respectively. The dielectric properties of the each material of samples are assumed to be independent with microwave frequency. The thermal and dielectric properties of the samples are shown in Table 1.

3. Mathematical formulations

Generally, studies on the microwave melting involve solutions of the equations governing electromagnetic propagation, i.e., Maxwell's equations, either by themselves or coupled with the heat transport equation. The surface of a sample is exposed to the monochromatic wave of TE_{10} mode with operating frequency of 2.45 GHz (shown as Fig. 2(a)).

3.1. Electromagnetic field equation

Fig. 2 shows the two-dimensional analytical model for microwave melting of a sample using a rectangular waveguide with a resonator. The proposed model is based on the following assumptions:

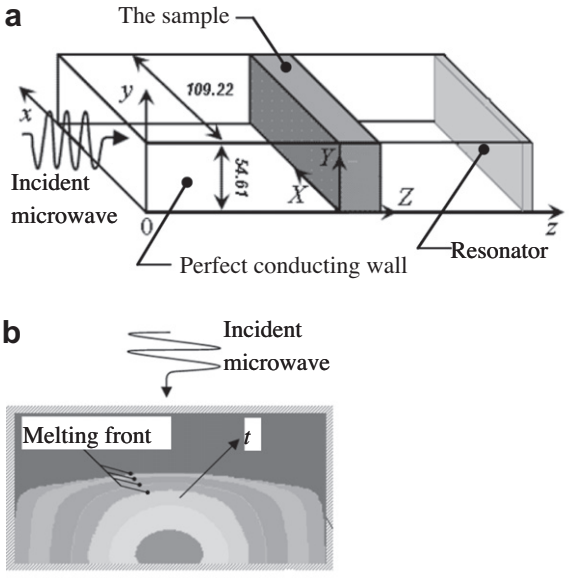

Fig. 2. The microwave system: (a) schematic of microwave system and (b) the physical model (in case of state (b)).

(1) Since the microwave field in the TE_{10} mode has no variation of field in the direction between the broad faces, a two-dimensional model over the x–z plane is applicable to analysis of electromagnetic field inside a rectangular waveguide [25].
(2) The absorption of microwave energy by the cavity (including air) in the rectangular waveguide is negligible.
(3) The walls of a rectangular waveguide are perfect conductors.
(4) The effect of the sample container on the electromagnetic field can be neglected.

The electromagnetic field is solved according to the theory of Maxwell's equations. In this study, the microwave of a fundamental TE_{10} mode is considered; therefore the Maxwell's equations in terms of the electric field intensity E and magnetic intensity H are given by:

$$\frac{\partial E_y}{\partial z} = \mu \frac{\partial H_x}{\partial t} \tag{1}$$

$$\frac{\partial E_y}{\partial x} = -\mu \frac{\partial H_z}{\partial t} \tag{2}$$

$$-\left(\frac{\partial H_z}{\partial x} - \frac{\partial H_x}{\partial z}\right) = \sigma E_y + \varepsilon \frac{\partial E_y}{\partial t} \tag{3}$$

where the permittivity ε, magnetic permeability μ and electric conductivity σ as:

$$\varepsilon = \varepsilon_0 \varepsilon_r, \quad \mu = \mu_0 \mu_r, \quad \sigma = 2\pi f \varepsilon \tan\delta \tag{4}$$

Additionally if magnetic effects are negligible, which is proven to be a valid assumption for most dielectric materials used in microwave heating applications, the magnetic permeability μ is well approximated by its value μ_0 in the free space. Let $\tan\delta$ is the loss tangent coefficient. In this work, the dielectric properties are assumed to vary with temperature only.

Boundary conditions: corresponding to the analytical mode as shown in Fig. 2, can be given as follows:

(a) Perfectly conducting boundaries. Boundary conditions on the inner wall surface of a rectangular waveguide are given by using Faraday's law and Gauss's theorem:

$$E_t = 0, \quad H_n = 0 \tag{5}$$

where subscripts t and n denote the components of tangential and normal directions, respectively.

(b) Continuity boundary condition. Boundary conditions along the interface between different materials, for example between air and dielectric material surface, are given by using Ampere's law and Gauss theorem:

$$E_t = E_t', \quad H_t = H_t', \quad D_n = D_n', \quad B_n = B_n' \tag{6}$$

where D is the electric flux density and B is the magnetic induction. The superscript $'$ denotes one of the different materials.

(c) Absorbing boundary condition. At the both ends of the rectangular waveguide, the first order absorbing conditions are applied [26]:

$$\frac{\partial E_y}{\partial t} = \pm \upsilon \frac{\partial E_y}{\partial z} \tag{7}$$

where ± represents forward or backward waves and υ is phase velocity of microwave. In case of installed resonator; the resonator boundary condition is applied at the end of rectangular waveguide:

$$E_y = 0, \quad H_z = 0 \tag{8}$$

(d) Oscillation of the electric and magnetic flied intensities by magnetron. Incident wave due to magnetron is given by the following equations:

$$E_y = E_{\text{yin}} \sin\left(\frac{\pi x}{L_x}\right) \sin(2\pi f t) \tag{9}$$

$$H_x = \frac{E_{\text{yin}}}{Z_H} \sin\left(\frac{\pi x}{L_x}\right) \sin(2\pi f t) \tag{10}$$

where E_{yin} is the input value of electric field intensity, L_x is the length of rectangular waveguide in x-direction and Z_H is the wave impedance defined as:

$$Z_H = \frac{\lambda_g Z_I}{\lambda} = \frac{\lambda_g}{\lambda}\sqrt{\frac{\mu}{\varepsilon}} \tag{11}$$

The power flux associated with a propagating electromagnetic wave is represented by the Poynting vector:

$$S = \frac{1}{2}\text{Re}(\vec{E} \times \vec{H}) \tag{12}$$

The Poynting theorem allows the evaluation of the microwave power input expressed as

$$P_{\text{in}} = \int_A S dA = \frac{A}{4Z_H} E_{\text{yin}}^2 \tag{13}$$

where Z_I denotes intrinsic impedance depending on the properties of the material. λ and λ_g are the wave lengths of microwaves in free space and rectangular waveguide, respectively.

3.2. Heat transport equation

The schematic of microwave system as displayed in Fig. 2(a). Initially, the walls are all insulated, and the sample is composed of a water-saturated porous medium (water and glass beads) and an ice-saturated porous medium (ice and glass beads), respectively. The temperature of the sample exposed to incident wave is obtained by solving the conventional heat transport equation with the microwave power absorbed included as a local electromagnetic energy term. In order to reduce complexity of the phenomena for analyze the process of heat transport due to microwave melting of a sample, several assumptions have been introduced into the heat equations as following assumptions:

(1) Corresponding to electromagnetic field, temperature field also can be assumed to be two-dimensional plane (x–z plane).
(2) The walls of sample are insulated.
(3) The effect of the container on temperature field can be neglected.
(4) The effect of the natural convection in the sample can be neglected.
(5) The local thermodynamic equilibrium along each phase is assumed.
(6) In this study, in a macroscopic sense, the pore structure within the material is assumed to be homogeneous and isotropic. Therefore, the heating model for a homogeneous and isotropic material is used in the current analysis.

The governing energy equations describing the temperature rise in a sample are the time dependent heat diffusion equation for two-dimensional heat flow with constant thermal properties for both the unfrozen and frozen layer, respectively as:

$$\frac{\partial T_l}{\partial t} = a_l\left(\frac{\partial^2 T_l}{\partial x^2} + \frac{\partial T_l}{\partial z^2}\right) + \frac{Q}{\rho \cdot C_p} + \frac{\partial T_l}{\partial z}\frac{dz}{dt} \tag{14}$$

$$\frac{\partial T_s}{\partial t} = a_s\left(\frac{\partial^2 T_s}{\partial x^2} + \frac{\partial^2 T_s}{\partial z^2}\right) + \frac{Q}{\rho \cdot C_p} + \frac{\partial T_s}{\partial z}\frac{dz}{dt} \tag{15}$$

where Q is local electromagnetic energy term, which is function of the electric field and defined [25] as

$$Q = 2\pi f \varepsilon_0 \varepsilon_r \tan\delta E_y^2 \tag{16}$$

Besides, last term of Eqs. (14) and (15) result from a coordinate transformation attached to moving boundary. In the unfrozen layer, internal convection can be neglected because the presence of glass beads minimizes the effect of natural convection current.

Boundary conditions:

(a) Adiabatic condition; assuming that the walls of the sample are insulate:

$$\frac{\partial T}{\partial n} = 0 \tag{17}$$

(b) Moving front boundary condition; the moving boundary between the unfrozen layer and frozen layer is described by the Stefan equation, which is obtained from a consideration of the energy balance at the interface between the unfrozen and frozen layer provides the following equation:

$$\left(\lambda_s \frac{\partial T_s}{\partial z} - q_{\mathrm{mov}} \Delta z_{\mathrm{mov}} - \lambda_l \frac{\partial T_l}{\partial z}\right)\left[1 + \left(\frac{\partial z_{\mathrm{mov}}}{\partial x}\right)^2\right] = \rho_s L_s \frac{\partial z_{\mathrm{mov}}}{\partial t} \tag{18}$$

where subscript mov denotes solid–liquid front (melting front), $\partial z_{\mathrm{mov}}/\partial t$ is the velocity of fusion front or melting front, and L_s the latent heat of fusion. To avoid changes in the physical dimensions as the melting front progresses, $\rho_s = \rho_l$ will be specified. In this study, the thermal conductivities, λ_l and λ_s are bulk-average values for the glass beads and the water or ice, respectively.

4. Grid generation

Generally, two types of structured grid generation are in used: algebraic method, i.e., transfinite or multivariate interpolation and partial differential equation mapping (PDE mapping) methods. Transfinite interpolation provides a relatively easy way of obtaining an initial grid that can be refined and smoothed by other methods, whether algebraic, PDE (this work), or variational method. For more complex geometries, such as this work, it is preferable to construct grid initially by transfinite interpolation, and to refine the grid filled in Cartesian coordinates in the interior of a domain by PDE mapping method subsequently.

4.1. Transfinite interpolation

The present method of constructing a two-dimensional boundary-conforming grid for a phase change in microwave melting is a direct algebraic approach based on the concept of transfinite interpolation. In this method, no partial differential equations are solved to obtain the curvilinear coordinates, and the same system is used for the entire domain. The algebraic method can be easier to construct than PDE mapping methods, and give easier control over grid characteristics such as orthogonality and grid point spacing. However, this method is sometime criticized for allowing discontinuities on the boundary to propagate into the interior and for not generating grids as smooth as those generated by PDE mapping method. The main idea behind this work, prior to generation of grids by PDE mapping methods, it is preferable to obtain first preliminary grids using the algebraic method, i.e., transfinite interpolation method. The combined transfinite interpolation and PDE mapping method is used to achieve a very smoother grids point distribution and boundary point discontinuities are smoothed out in the interior domain.

For the concept of transfinite interpolation, a significant extension of the original formulation by Gordon and Hall [21] has made, it is possible to initially generate global grid system with geometry specifications only on the outer boundaries of the computation domain and yet obtain a high degree of local control. Moreover, to successfully track the moving boundary front, the grid generation mapping must adapt to large deformations of the interface shape while maintaining as much orthogonality and smoothness as possible. Due to the generality of the method it has been possible to use more advanced mappings than conventional types and thereby improve the overall efficiency of the grid in term of computational work for a given resolution.

In Fig. 3, the present method of constructing a two-dimensional boundary-conforming grid for a system, which it is a direct algebraic approach based on the concept of transfinite or multivariate interpolation. It is possible to initially generate global single plane transformations with geometry specifications only on outer boundaries of the computational domain.

Let $f(u, w) = (x(u, w), z(u, w))$ denote a vector-valued function of two parameters u, w defined on the region $u_1 \leqslant u \leqslant u_{\max}$, $w_1 \leqslant w \leqslant w_{\max}$. This function is not known throughout the region, only on certain planes (Fig. 3). The transfinite interpolation procedure then gives the interpolation function $f(u, w)$ by the recursive algorithm [24]:

$$\begin{aligned} f^{(1)}(u,w) &= A_1(u)\cdot f(1,w) + A_2(u)\cdot f(u_{\max},w) \\ f(u,w) &= f^{(1)}(u,w) + B_1(w)\cdot[f(u,1) - f^{(1)}(u,1)] \\ &\quad + B_{2(w)}\cdot[f(u,w_{\max}) - f^{(1)}(u,w_{\max})] \end{aligned} \tag{19}$$

where $A_1(u)$, $A_2(u)$, $B_1(w)$ and $B_2(w)$ are defined the set of univariate blending functions, which only have to satisfy the conditions:

$$\begin{aligned} &A_1(1) = 1, \quad A_1(u_{\max}) = 0, \quad A_2(1) = 0, \quad A_2(u_{\max}) = 1 \\ &B_1(1) = 1, \quad B_1(u_{\max}) = 0, \quad B_2(1) = 0, \quad B_2(u_{\max}) = 1 \end{aligned}$$

Further, the general form in algebraic equations can be defined as:

$$\begin{aligned} A_1(u) &= \frac{u_{\max} - u}{u_{\max} - 1}, \quad A_2(u) = 1 - A_1(u), \\ B_1(w) &= \frac{w_{\max} - w}{w_{\max} - 1}, \quad B_2(w) = 1 - B_1(w) \end{aligned} \tag{20}$$

The grid motion defined from a moving boundary motion is modeled using a Stefan equation (Eq. (18)) with a transfinite mapping method. Furthermore, the boundary fitted grid generation mapping discussed in this section forms the basis for the interface tracking mapping. However, the mapping must now match the interface curve on the interior of physical domain in addition to fitting the outer physical boundary. In addition, the system must be adaptive since the grid lines must change to follow the deforming interface while maintaining as much smoothness and orthogonality as possible.

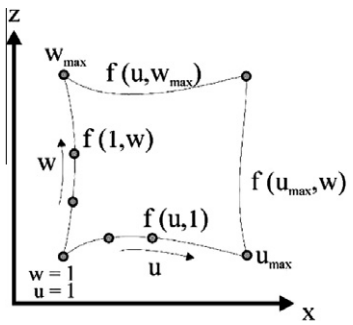

Fig. 3. The parametric domain with $f(u, w)$ specified on planes of constant u, w.

4.2. PDE mapping

In the proposed grid generation mapping, all grids discussed and displayed have been couched in terms of finite difference algorithm applications, with the understanding that whatever non-uniform grid exists in the physical space, there is exist a transformation which will recast it as a uniform rectangular grid in the computational space. The finite difference calculations are then made over this uniform grid in the computational space, after which the field results are transferred directly back to the corresponding points in the physical space. The purpose of generating a smooth grid that conforms to physical boundaries of problem is, of course, to solve the partial differential equations specified in the problem by finite difference scheme, capable of handling general non-orthogonal curvilinear coordinates.

Corresponding to Fig. 2(b), as melting proceeds, a melting front denoted here z_{mov} is formed. Due to the existence of this melting front, the frozen and unfrozen domains are irregular and time dependent. To avoid this difficulty, a curvilinear system of coordinates is used to transform the physical domain into rectangular region for the computational domain.

It is convenient to introduce a general curvilinear coordinate system as follows Anderson [27]:

$$x = x(\xi,\eta), \quad z = z(\xi,\eta) \text{ or } \xi = \xi(x,z), \quad \eta = \eta(x,z) \tag{21}$$

The moving boundaries are immobilized in the dimensionless (ξ,η) coordinate for all times. With the details omitted, then the transformation of electromagnetic field equation (Eqs. (1), (2), (3), and (7)) can be written respectively as [10]:

$$\frac{1}{J}\left(x_\xi \frac{\partial E_y}{\partial \eta}\right) = \mu \frac{\partial H_x}{\partial t} \tag{22}$$

$$-\frac{1}{J}\left(z_\eta \frac{\partial E_y}{\partial \xi}\right) - z_\xi \frac{\partial E_y}{\partial \eta} = -\mu \frac{\partial H_z}{\partial t} \tag{23}$$

$$-\frac{1}{j}\left\{\left(z_\eta \frac{\partial H_z}{\partial \xi} - z_\xi \frac{\partial H_z}{\partial \eta}\right) - \left(x_\xi \frac{\partial H_x}{\partial \eta}\right)\right\} = \sigma E_y + \varepsilon \frac{\partial E_y}{\partial t} \tag{24}$$

$$\frac{\partial E_y}{\partial t} = \upsilon \frac{1}{J}\left(x_\xi \frac{\partial E_y}{\partial \eta}\right) \tag{25}$$

Also the heat transport equations (Eqs. (14) and (15)), and Stefan condition (Eq. (18)) can be transformed into (ξ,η) coordinate as below:

$$\begin{aligned}\frac{\partial T_l}{\partial t} &= \frac{a_l}{J^2}\left(\alpha \frac{\partial^2 T_l}{\partial \xi^2} - 2\beta \frac{\partial^2 T_l}{\partial \xi \partial \eta} + \gamma \frac{\partial^2 T_l}{\partial \eta^2}\right) \\ &+ \frac{a_l}{J^3}\left[\left(\alpha \frac{\partial^2 x}{\partial \xi^2}\right)\left(z_\xi \frac{\partial T_l}{\partial \eta} - z_\eta \frac{\partial T_l}{\partial \xi}\right)\right. \\ &\left. + \left(\alpha \frac{\partial^2 z}{\partial \xi^2} - 2\beta \frac{\partial^2 z}{\partial \xi \partial \eta} + \gamma \frac{\partial^2 z}{\partial \eta^2}\right)\left(-x_\xi \frac{\partial T_l}{\partial \eta}\right)\right] \\ &+ \frac{Q}{\rho \cdot C_p} + \frac{1}{J}\left(x_\xi \frac{\partial T_l}{\partial \eta}\right)\frac{dz}{dt}\end{aligned} \tag{26}$$

$$\begin{aligned}\frac{\partial T_s}{\partial t} &= \frac{a_s}{J^2}\left(\alpha \frac{\partial^2 T_s}{\partial \xi^2} - 2\beta \frac{\partial^2 T_s}{\partial \xi \partial \eta} + \gamma \frac{\partial^2 T_s}{\partial \eta^2}\right) \\ &+ \frac{a_s}{J^3}\left[\left(\alpha \frac{\partial^2 x}{\partial \xi^2}\right)\left(z_\xi \frac{\partial T_s}{\partial \eta} - z_\eta \frac{\partial z}{\partial \xi}\right)\right. \\ &\left. + \left(\alpha \frac{\partial^2 z}{\partial \xi^2} - 2\beta \frac{\partial^2 z}{\partial \xi \partial \eta} + \gamma \frac{\partial^2 z}{\partial \eta^2}\right)\left(-x_\xi \frac{\partial T_s}{\partial \eta}\right)\right] \\ &+ \frac{Q}{\rho \cdot C_p} + \frac{1}{J}\left(x_\xi \frac{\partial T_s}{\partial \eta}\right)\frac{dz}{dt}\end{aligned} \tag{27}$$

$$\begin{aligned}&\left\{\lambda_s \frac{1}{J}\left(x_\xi \frac{\partial T_s}{\partial \eta}\right) - \lambda_l \frac{1}{J}\left(x_\xi \frac{\partial T_l}{\partial \eta}\right)\right\}\left\{1 + \left(\frac{1}{J}\left[z_\eta \frac{\partial z_{mov}}{\partial \xi} - z_\xi \frac{\partial z_{mov}}{\partial \eta}\right]\right)^2\right\} \\ &= \rho_s L_s \frac{\partial z_{mov}}{\partial t}\end{aligned} \tag{28}$$

where $J = x_\xi \cdot z_\eta - x_\eta \cdot z_\xi$, $\alpha = x_\eta^2 + z_\eta^2$, $\beta = x_\xi \cdot x_\eta + z_\xi \cdot z_\eta$, $\gamma = x_\xi^2 + z_\xi^2$ and, x_ξ, x_η, z_ξ and z_η denote partial derivatives, J is the Jacobian, β, α, γ are the geometric factors and η, ξ are the transformed coordinates [27].

5. Solution method

It is known that the inherent difficulties in the conventional numerical methods (pure parabolic grid generators) for melting or freezing problems suggest the use of combined transfinite interpolation and PDE methods in most instances. Although conventional numerical methods can be used to obtain satisfactory results, there are problems of large time consumption and control functions that are often difficult to determine. Therefore, the new method presented in this paper is generally preferable because it offers the highest overall accuracies and smooth grid point distribution. In addition, the boundary point discontinuities are smoothed out in the interior domain and orthogonality at boundaries can be maintained.

During the solving of a moving boundary problem including phase change in microwave melting process, complications arise due to the motion of melting front with elapsed time. In this study, the description of heat transport equations (Eqs. (14) and (15)) requires specification of the temperature T in sample layers and moving front boundary is solved. Theses equations are coupled to the Maxwell's equations (Eqs. (1)–(3)) by Eq. (16). The latter equation represents the heating effect of microwaves in both the unfrozen and frozen layer. Therefore, the numerical schemes of the microwave melting process are performed.

5.1. Electromagnetic field discretization

Generally, simulation of microwave power dissipation requires the solution of the set of three coupled scalar partial differential equations governing electromagnetic propagation, i.e., Maxwell's equation, inside a rectangular waveguide. The finite difference time-domain (FDTD) method has been used to provide a full description of electromagnetic scattering and absorption and give detailed spatial and temporal information of wave propagation.

In this study, the leapfrog scheme is applied to a set of Maxwell's equations. The electric field vector components are offset one half-cell in the direction of their corresponding components, while the magnetic field vector components are offset one half-cell in each direction orthogonal to their corresponding components [28]. The electric and magnetic fields are evaluated at alternative half time steps. For TE_{10} mode, the electric and magnetic field components are expressed by the total field FDTD equations as

$$\begin{aligned}E_y^n(k,i) &= \frac{1 - \frac{\sigma(k,i)\Delta t}{2\varepsilon(k,i)}}{1 + \frac{\sigma(k,i)\Delta t}{2\varepsilon(k,i)}} E_y^{n-1}(k,i) \\ &+ \frac{1}{1 + \frac{\sigma(k,i)\Delta t}{2\varepsilon(k,i)}} \times \frac{\Delta t}{\varepsilon(k,i) J(k,i)} \left\{\frac{z(k,i+1) - z(k,i-1)}{2\Delta \xi}\right. \\ &\times \frac{\left(H_z^{n-1/2}(k,i+1/2) - H_z^{n-1/2}(k,i-1/2)\right)}{\Delta \eta} \\ &- \frac{z(k+1,i) - z(k-1,i)}{2\Delta \eta} \\ &\left. \times \frac{\left(H_z^{n-1/2}(k+1/2,i) - H_z^{n-1/2}(k+1/2,i)\right)}{\Delta \xi}\right.\end{aligned}$$

$$+\frac{x(k,i+1)-x(k,i-1)}{2\Delta\xi}\times\frac{\left(H_x^{n-1/2}(k+1/2,i)-H_z^{n-1/2}(k-1/2,i)\right)}{\Delta\eta}\Bigg\} \quad (29)$$

$$H_x^{n+1/2}(k+1/2,i)=H_x^{n-1/2}(k+1/2,i)+\frac{\Delta t}{\mu(k+1/2,i)J(k+1/2,i)}\times\left\{\frac{x(k+1/2,i-1)-x(k+1/2,i+1)}{2\Delta\xi}\times\frac{E_y^n(k+1,i)-E_y^n(k,i)}{\Delta\eta}\right\} \quad (30)$$

$$H_z^{n+1/2}(k,i+1/2)=H_z^{n-1/2}(k,i+1/2)-\frac{\Delta t}{\mu(k,i+1/2)J(k,i+1/2)}\left\{\frac{z(k+1,i+1/2)-z(k-1,i+1/2)}{\Delta\eta}\times\frac{E_y^n(k,i+1)-E_y^n(k,i)}{\Delta\xi}-\frac{z(k,i+3/2)-z(k,i-1/2)}{\Delta\xi}\times\frac{E_y^n(k+1,i)-E_y^n(k,i)}{\Delta\eta}\right\} \quad (31)$$

5.2. Heat transport discretization

The transient heat equation (Eqs. (14) and (15)) and the Stefan condition (Eq. (18)) are solved by using finite difference method. A system of nonlinear equations results whereby each equation for the internal nodes can be cast into a numerical discretization, as shown below;

In transient heat equation for unfrozen layer,

$$\begin{aligned}T_l^{n+1}(k,i)=&\frac{1}{1+\frac{2a_l\Delta t}{J^2(k,i)}\left(\frac{\alpha(k,i)}{\Delta\xi\Delta\xi}+\frac{\gamma(k,i)}{\Delta\eta\Delta\eta}\right)}\\&\times\Bigg\{T_l^n(k,i)+\frac{a_l\Delta t}{J^2(k,i)}\Bigg[\alpha(k,i)\frac{T_l^{n-1}(k,i+1)+T_l^{n+1}(k,i-1)}{\Delta\xi\Delta\xi}\\&-2\beta(k,i)\left(\frac{T_l^{n-1}(k+1,i+1)-T_l^{n+1}(k-1,i+1)}{2\Delta\eta}-\frac{T_l^{n-1}(k+1,i-1)-T_l^{n+1}(k-1,i-1)}{2\Delta\xi}\right)\Bigg/\\&2\Delta\xi+\gamma(k,i)\frac{T_l^{n-1}(k+1,i)+T_l^{n+1}(k-1,i)}{\Delta\eta\Delta\eta}\Bigg]\\&+\frac{a_l\Delta t}{J^3(k,i)}\Bigg[\alpha(k,i)\frac{X(k,i+1)-2X(k,i)+X(k,i-1)}{\Delta\xi\Delta\xi}\\&\times\left(\frac{Z(k,i+1)-Z(k,i-1)}{2\Delta\xi}\times\frac{T_l^{n-1}(k+1,i)-T_l^{n+1}(k-1,i)}{2\Delta\eta}-\frac{Z(k+1,i)-Z(k-1,i)}{2\Delta\eta}\times\frac{T_l^{n-1}(k,i+1)-T_l^{n+1}(k,i-1)}{2\Delta\xi}\right)\\&+\Bigg(\alpha(k,i)\frac{Z(k,i+1)-2Z(k,i)+Z(k,i-1)}{\Delta\xi\Delta\xi}\\&-2\beta(k,i)\left(\frac{Z(k+1,i+1)-Z(k-1,i+1)}{2\Delta\eta}-\frac{Z(k+1,i-1)-Z(k-1,i-1)}{2\Delta\eta}\right)\Bigg/\\&2\Delta\xi+\gamma(k,i)\left(\frac{Z(k+1,i)-2Z(k,i)+Z(k-1,i)}{\Delta\eta\Delta\eta}\right)\\&\times\left(-\frac{X(k,i+1)-X(k,i-1)}{2\Delta\xi}\right)\\&\times\left(\frac{T_l^n(k+1,i)-T_l^n(k-1,i)}{2\Delta\eta}\right)\Bigg]+\frac{Q\Delta t}{\rho C_p}\\&+\frac{1}{J(k,i)}\left(\frac{X(k,i+1)-X(k,i-1)}{2\Delta\xi}\right)\\&\times\left(\frac{T_l^n(k+1,i)-T_l^n(k-1,i)}{2\Delta\eta}\right)\times\Delta z\Bigg\}\end{aligned} \quad (32)$$

In transient heat equation for frozen layer,

$$\begin{aligned}T_s^{n+1}(k,i)=&\frac{1}{1+\frac{2a_l\Delta t}{J^2(k,i)}\left(\frac{\alpha(k,i)}{\Delta\xi\Delta\xi}+\frac{\gamma(k,i)}{\Delta\eta\Delta\eta}\right)}\\&\times\Bigg\{T_s^n(k,i)+\frac{a_l\Delta t}{J^2(k,i)}\Bigg[\alpha(k,i)\frac{T_s^{n-1}(k,i+1)+T_s^{n+1}(k,i-1)}{\Delta\xi\Delta\xi}\\&-2\beta(k,i)\left(\frac{T_s^{n-1}(k+1,i+1)-T_s^{n+1}(k-1,i+1)}{2\Delta\eta}-\frac{T_s^{n-1}(k+1,i-1)-T_s^{n+1}(k-1,i-1)}{2\Delta\xi}\right)\Bigg/\\&2\Delta\xi+\gamma(k,i)\frac{T_s^{n-1}(k+1,i)+T_s^{n+1}(k-1,i)}{\Delta\eta\Delta\eta}\Bigg]\\&+\frac{a_l\Delta t}{J^3(k,i)}\Bigg[\alpha(k,i)\frac{X(k,i+1)-2X(k,i)+X(k,i-1)}{\Delta\xi\Delta\xi}\\&\times\left(\frac{Z(k,i+1)-Z(k,i-1)}{2\Delta\xi}\times\frac{T_s^{n-1}(k+1,i)-T_s^{n+1}(k-1,i)}{2\Delta\eta}-\frac{Z(k+1,i)-Z(k-1,i)}{2\Delta\eta}\times\frac{T_s^{n-1}(k,i+1)-T_s^{n+1}(k,i-1)}{2\Delta\xi}\right)\\&+\Bigg(\alpha(k,i)\frac{Z(k,i+1)+2Z(k,i)-Z(k,i-1)}{\Delta\xi\Delta\xi}\\&-2\beta(k,i)\left(\frac{Z(k+1,i+1)-Z(k-1,i+1)}{2\Delta\eta}-\frac{Z(k+1,i-1)-Z(k-1,i-1)}{2\Delta\eta}\right)\Bigg/2\Delta\xi\\&+\gamma(k,i)\frac{Z(k+1,i)-2Z(k,i)+Z(k-1,i)}{\Delta\eta\Delta\eta}\Bigg)\\&\times\left(-\frac{X(k,i+1)-X(k,i-1)}{2\Delta\xi}\right)\\&\times\left(\frac{T_s^n(k+1,i)-T_s^n(k-1,i)}{2\Delta\eta}\right)\Bigg]+\frac{Q\Delta t}{\rho C_p}\\&+\frac{1}{J(k,i)}\left(\frac{X(k,i+1)-X(k,i-1)}{2\Delta\xi}\right)\\&\times\left(\frac{T_s^n(k+1,i)-T_l^n(k-1,i)}{2\Delta\eta}\right)\times\Delta z\Bigg\}\end{aligned} \quad (33)$$

In Stefan condition,

$$\begin{aligned}Z^{n+1}(k,i)=&Z^n(k,i)+\frac{\Delta T}{\rho_s L_s}\Bigg\{\Bigg[\frac{\lambda_s}{J(k+1,i)}\\&\times\left(\frac{X(k+1,i+1)-X(k+1,i-1)}{2\Delta\xi}\right)\\&\times\left(\frac{-3T_s(k,i)+4T_s(k+1,i)-T_s(k+2,i)}{2\Delta\eta}\right)\\&-\frac{\lambda_l}{J(k-1,i)}\times\left(\frac{X(k-1,i+1)-X(k-1,i-1)}{2\Delta\xi}\right)\\&\times\left(\frac{3T_l(k,i)-4T_l(k-1,i)+T_l(k-2,i)}{2\Delta\eta}\right)\Bigg]\\&\times\left[1+\left(\begin{array}{c}\frac{Z^n(k+1,i)-Z^n(k-1,i)}{2\Delta\eta}\times\frac{Z^n(k+1,i)-Z^n(k-1,i)}{2\Delta\xi}\\-\frac{Z^n(k,i+1)-Z^n(k,i-1)}{2\Delta\xi}\times\frac{Z^n(k,i+1)-Z^n(k,i-1)}{2\Delta\eta}\end{array}\right)^2\right]\Bigg\}\end{aligned} \quad (34)$$

The details of computational schemes and strategy for solving the combined transfinite interpolation functions (Eqs. (19) and (20)) and PDE mapping (Eqs. (29)–(34)) are illustrated in Fig. 4.

5.3. The stability and accuracy of calculation

Due to dielectric properties of the most liquids are depending on temperature so it is necessary to consider the coupling model for analysing the E field and the temperature distribution. For this reason, the iteration scheme (reference from Ratanadecho et al. [10]) is used to resolve the non-linear coupling of Maxwell's equations, and energy equations. Spatial and temporal resolution is selected to ensure of stability and accuracy. To insure stability of the time-stepping algorithm Δt is chosen to satisfy the courant stability condition [25]:

$$\Delta t \leqslant \frac{\sqrt{(\Delta x)^2 + (\Delta z)^2}}{\upsilon} \tag{35}$$

And the spatial resolution of each cell defines as:

$$\Delta x, \Delta z \leqslant \frac{\lambda_g}{10\sqrt{\varepsilon_r}} \tag{36}$$

where υ is the velocity of an electromagnetic wave. Corresponding to Eqs. (35) and (36), the calculations are as follows:

(1) Initial grid size: $\Delta x = 1.0922$ mm and $\Delta z = 1.0000$ mm.
(2) Time steps: $\Delta t = 2 \times 10^{-12}$ s and $\Delta t = 1.0$ s are used corresponding to electromagnetic field, and temperature field calculations and location of melting front, respectively.
(3) Relative error in the iteration procedures of 10^{-6} is chosen.

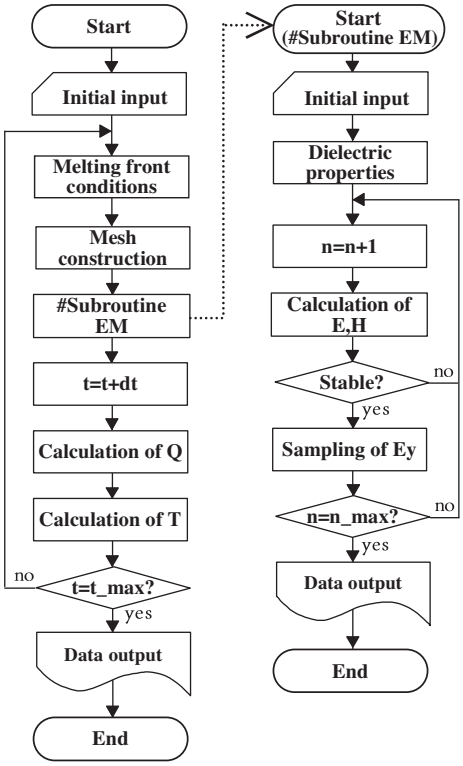

Fig. 4. The computational scheme.

6. Results and discussion

The present work is to couple the grid generation algorithm with electromagnetic field and heat transport equations. The thermal analysis during melting process will be discussed in next subsection.

6.1. Physical description

The sample is composed of an unfrozen layer (water and glass bead) and a frozen layer (ice and glass bead). The unfrozen layer and the frozen layer are arranged in different configurations, as shown in state (a) and state (b) of Fig. 1(b), respectively. It is considered to illustrate microwave melting phenomena by using a rectangular waveguide incase of with and without resonator. In

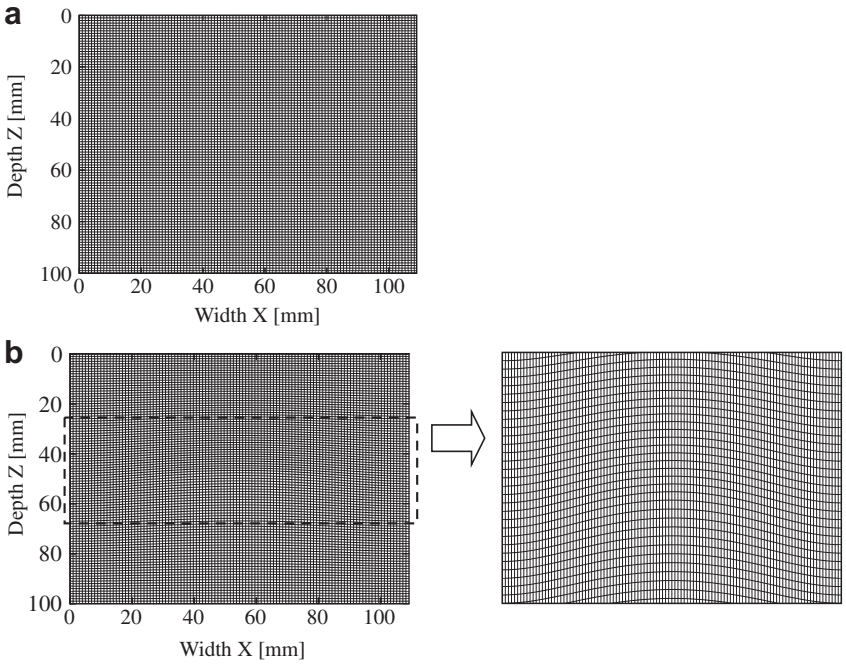

Fig. 5. Grid simulating the deformation of an interface: (a) the initial reference grid for the domain (generated by pure transfinite interpolation method) and (b) melting time of 60 s.

case of without a resonator, all transmitted waves through the sample are absorbed by fixed water load at end of the waveguide (lower boundary condition). Unlike for the case with resonator that perfectly conducting plate is installed at the end of waveguide to enhance resonance of standing wave inside a rectangular waveguide as well as the sample.

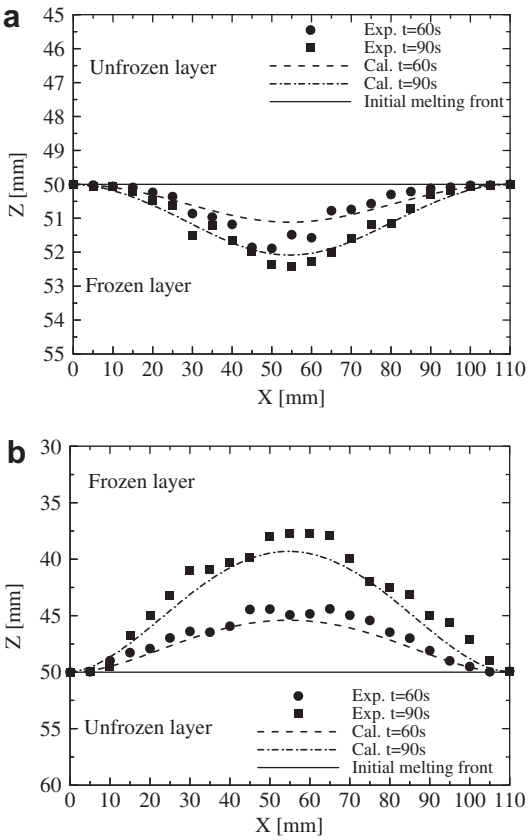

Fig. 6. The measured and predicted interface position: (a) melting front for state (a) and (b) melting front for state (b).

6.2. A melting front tracking grid generation system

The efficiency of the grid generation system is illustrated during the melting of ice-saturated porous medium (porosity, $\phi = 0.38$) subjected to electromagnetic energy. Fig. 5(a) shows the initial reference grid for the domain generated by pure transfinite interpolation method. Fig. 5(b) shows grid that fit curves that are typical of shapes seen during deformation of an interface with respect to elapsed time at $t = 60$ s. The calculated front locations correspond to the initial temperature of 0 °C and supplied microwave power level of 1000 W. It is found that the grid is able to maintain a significant amount of orthogonality and smoothness both within the interior and along the boundary as the grid points redistribute themselves to follow the interface. These results show the efficiency of the present method for the multi-dimensional moving boundary problem.

6.3. Numerical validation

Fig. 6(a) and (b) shows the present simulation results compared with experimental data of melting front within the layered sample without resonator in which state (a) and state (b), corresponding to the initial temperature of 0 °C for both a frozen layer and an unfrozen layer.

It is observed that the trends of results are in good agreement. However, at longer melting times (90 s) in case of state (b), the experimental data is significantly higher than that the simulation results. The source of the discrepancy is the non-uniform heating effect along the axis, which accounts for the fact that the incident microwave at the surface of a layered sample is non-uniform. Numerically, the discrepancy may be attributed to uncertainties in the thermal and dielectric property database, and the mechanism of natural convective heat transfer is not considered. On the other hand during the experiment of microwave melting process, the impact on the uncertainty of our data may cause by variations in humidity, room temperature and another effects. The uncertainty in melting kinetics was assumed to result from errors in the measured melting front of the sample.

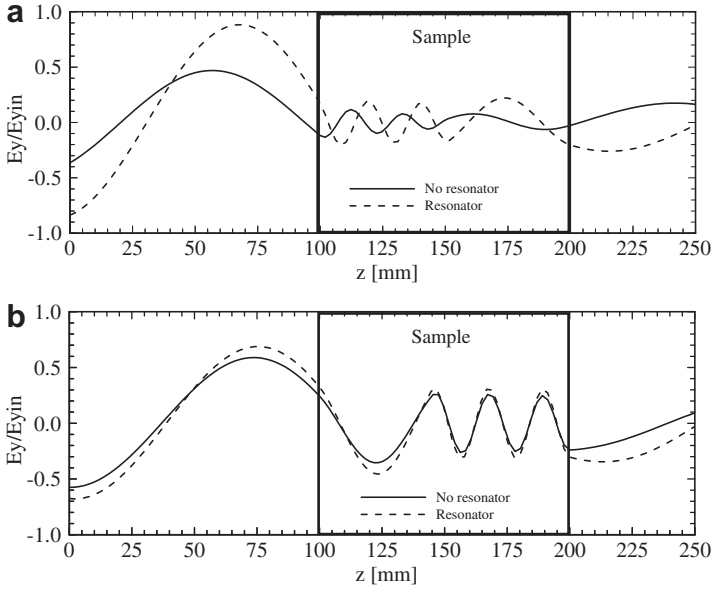

Fig. 7. Electric field distribution at $t = 60$ s: (a) state-a and (b) state-b.

6.4. Electric field distribution

Fig. 7(a) and (b) illustrates the electric field distribution along the center axis (x = 54.6 mm) of rectangular waveguide at t = 60 s for different sample configuration as state (a) and state (b), in case of with and without resonator. In these figures, the vertical axis represents the intensity of the electric fields E_y, which is normalized to the amplitude of the input electric fields E_{yin}. A solid line represents the electric fields distribution inside a rectangular waveguide for the cases without resonator; all transmitted waves through the sample are absorbed by water load at the end of the waveguide. Since the sample is composed of the unfrozen layer and frozen layer. In addition, the unfrozen layer is a highly absorptive material (higher dielectric loss factor) while the frozen layer is a highly transparent material (low dielectric loss factor), where a larger part of microwave is able to transmit through this layer. For the case of state (a), the unfrozen layer considered as high lossy material has a short wavelength, which correspond to higher microwave power absorbed. It is observed from the figures that the resonance of standing wave configuration inside the sample is weak as compared to left-hand side of the sample. The some part of microwave is transmitted through the sample and then absorbed by water load at the end of the waveguide. Focusing attention of electric field distribution inside the cavity (left-hand side), a stronger standing wave with large amplitude is formed by interference between the incident and reflected waves from the surface of the sample due to the different dielectric properties of materials (air and sample) at this interface. It is evident from the results that the electric field within the sample attenuates owing to the microwave power absorbed, and thereafter the microwave power absorbed is converted to the thermal energy. In case of state (b), it is similar to state (a) that a larger part of microwaves is absorbed by the unfrozen layer. In addition, a stronger standing wave with large amplitude is formed inside the cavity (left-hand side) by interference between the incident and reflected waves from surface of the sample. Note that the amplitude of electric field inside cavity (left-hand side) of state (b) is lower than state (a) because the upper surface of the frozen layer in state (b) (exposed to incident microwaves) is a highly transparent and it protects the reflected wave from this surface.

For the cases with installed a resonator in the waveguide on both state (a) and state (b), the electric fields with small amplitude are formed within the sample, while the stronger standing wave outside the sample (left-hand side) with a lager amplitude is formed by among the forward wave, the reflected wave from the sample and the resonator. However, due to the reflections occurring at air-resonator interface, the standing wave can be also formed at the right-hand side of the sample as seen in the figure. It is interesting to observe that the electric field intensity in case of with resonator is greater than in case of without resonator for both different sample configurations as state (a) and state (b). In addition, the electric field within the sample attenuates owing to microwave power absorbed, and thereafter the microwave power absorbed is converted to thermal energy (similar to case without resonator).

6.5. Melting process without resonator

This section is presented to examine the melting characteristics of the layered sample for state (a) and state (b) configuration, respectively.

6.5.1. The temperature and microwave power absorbed distribution

Fig. 8(a) shows temperature distribution of state (a). It is observed that the skin-depth heating effect causes a major part of incident waves to be absorbed within the sample, especially at the leading edge of an unfrozen layer. The temperature distribution corresponds to the electric distribution in the sample. This is because the electric field within the sample attenuates owing to microwave power absorbed, and thereafter the microwave power absorbed is converted to thermal energy where the maximum temperature occurs at leading edge of unfrozen layer. It is observed that temperature distribution within the unfrozen layer display a wavy behavior while it has no temperature gradient in the frozen layer due to this layer acts as the transparent material (very low lossy material). In addition, corresponding to the microwave power absorbed as displayed in Fig. 8(c), the temperature distribution within the unfrozen layer decays slowly along the wave propagation direction.

Fig. 8(b) and (d) illustrates the results of state (b). The incident microwave is easily further penetrated to the unfrozen layer, which forms a highly absorptive material. Since an ice in the frozen

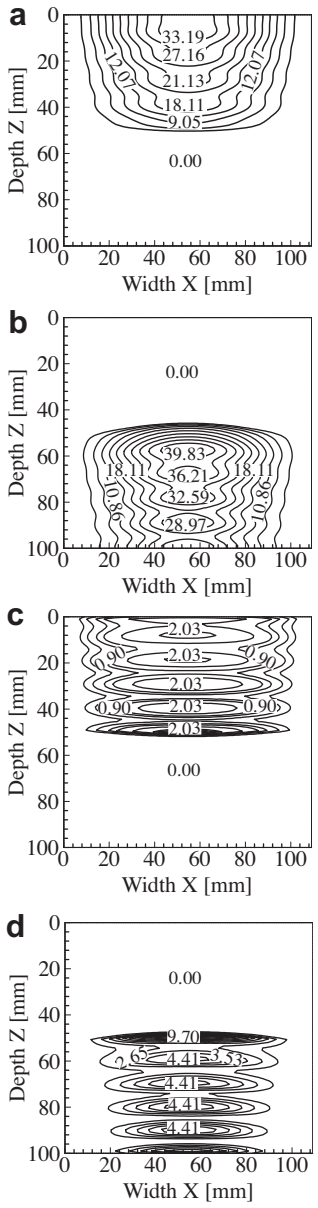

Fig. 8. Temperature and microwave power absorbed distribution at t = 60 s (without resonator): (a) temperature of state-a, (b) temperature of state-b, (c) microwave power absorbed of state-a and (d) microwave power absorbed of state-b.

layer is a highly transparent material to microwave where it protects the reflective wave from the expose surface. The latter arises from the fact that the larger part of microwaves can be absorbed at the leading edge of the unfrozen layer. The presence of the strength of microwave power absorbed gives to rise a hot spot at the leading edge of the unfrozen layer. This causes heat to conduct from the hotter region in unfrozen layer (higher microwave power absorbed) to the cooler region (lower microwave power absorbed) in the frozen layer. It is found that the upward movement of melting front occurs at the interface between frozen layer and unfrozen layer where the strength of the microwave power absorbed increases with increasing the melting rate. As melting proceed, the melting rate is higher in comparison to previous case (state (a)) at the same time. Nevertheless, the frozen layer stays colder due to the difference between the dielectric properties of water and ice. This is because water is a highly absorptive material, while ice is highly transparent which results in a lower microwave power absorbed within this layer. At exposure time of about 60 s, there is a difference of about 39.83 °C between the maximum and minimum temperatures.

6.5.2. Melting front

Considerately, Fig. 6 shows the melting front for the case of state (a) and state (b). For state (a), melting front moves slowly with the elapsed time along the propagation direction because the most of heat as well as microwave power absorbed take place at leading edge of unfrozen layer, which located far away from frozen layer. Consequently, a small amount of heat can conduct to the frozen layer because the water layer downstream acts as an insulator causing a slow movement of melting front. In state (b), in contrast to that state (a), the melting front moves rapidly with the elapsed time against the wave propagating direction. This is because the most of the heat directly conduct into the frozen layer due to the fact that the hot spot takes place at the leading edge of the unfrozen layer which located close to the frozen layer.

6.6. Melting process with resonator

Fig. 9 illustrates the temperature and microwave power absorbed distribution in case of with installed resonator at the end of waveguide. The temperature distribution corresponds to the electric distribution in the sample. This is because the electric field within the sample attenuates owing to microwave power absorbed, and thereafter the microwave power absorbed is converted to thermal energy as explained in previous subsection. It is observed that temperature distribution within the unfrozen layer display a stronger wavy behavior similarly case of without resonator. Since the microwaves can either transmit through sample or reflect from resonator, a standing wave or resonance is formed within the

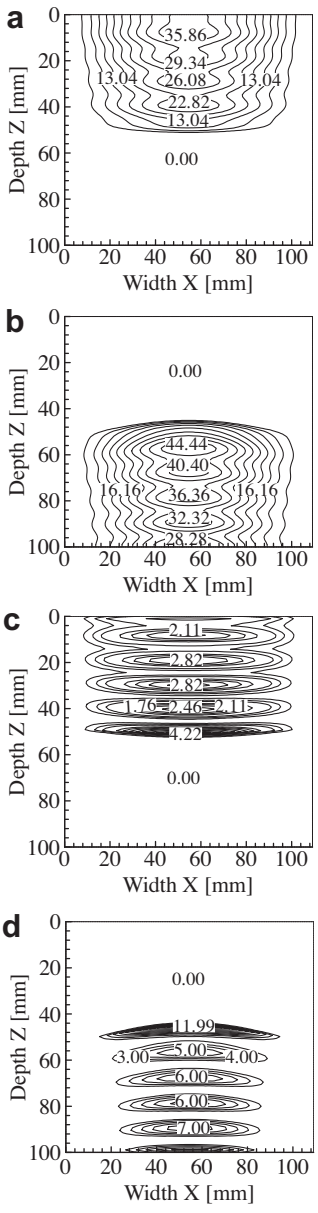

Fig. 9. Temperature and microwave power absorbed distribution at $t = 60$ s (with resonator): (a) temperature of state-a, (b) temperature of state-b, (c) microwave power absorbed of state-a and (d) microwave power absorbed of state-b.

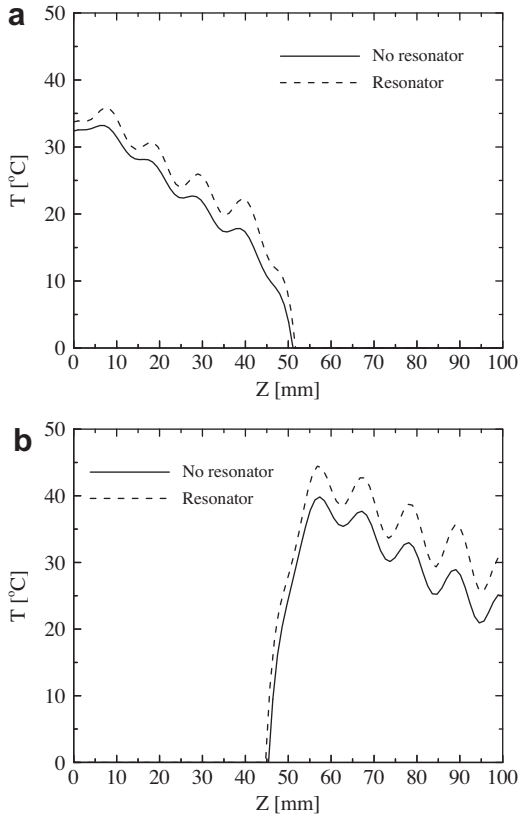

Fig. 10. Temperature profile along z-axis within the sample at $t = 60$ s: (a) state-a and (b) state-b.

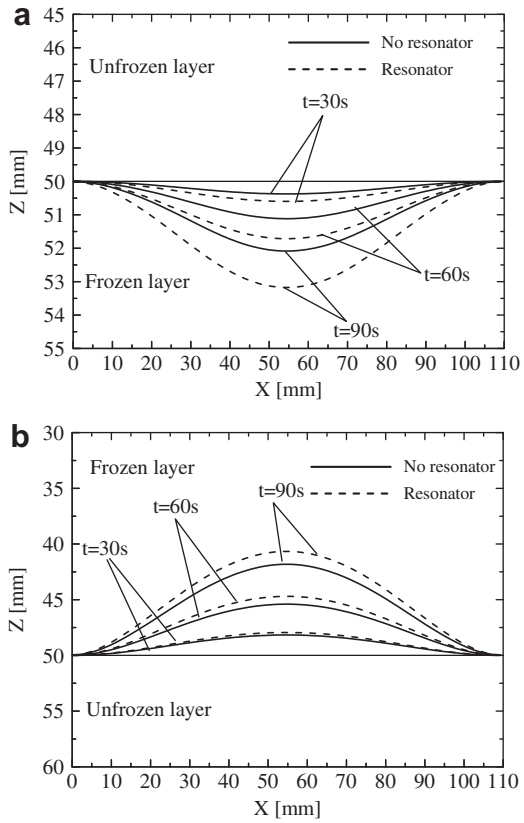

Fig. 11. Melting front at various elapsed times: (a) state-a and (b) state-b.

sample. Therefore, the microwave power absorbed as well as heat transfer rate in the sample is stronger greater than that case of without resonator. At exposure time of about 60 s, there is a difference between the maximum and minimum temperatures of about 35.86 °C and 44.44 °C, for state (a) and state (b), respectively.

Furthermore, it is interesting that the temperature profiles along the center axis (x = 54.6 mm) is greater than that case of without resonator as shown in Fig. 10. These results combined that the installation of resonator can lead to enhance a stronger standing wave or resonance.

Fig. 11 shows the results of melting front in state (a) and state (b), respectively. For the case of installed resonator, the temperature and the microwave power absorbed are always higher when compared with case of without resonator. Thus, the melting front rapidly moves with elapsed times in comparison to case of no-resonator condition. Additionally, it is interesting that melting rate of state (a) is greater than state (b) because of the difference in standing wave pattern and microwave power absorbed within sample.

This study shows the capability of the present method to correctly handle the phase change problem. With further quantitative validation of the present method, this method can be used as a tool for investigating in detail this particular melting of phase change in a porous media at a fundamental level.

7. Conclusions

Mesh quality has the largest impact on solution quality. A high-quality mesh increases the accuracy of the computational thermal flow solution and improves convergence. Therefore, it is important to provide tools for obtaining and improving a mesh. This paper present, melting of ice-saturated porous medium in a rectangular waveguide (with and without resonator) subjected to electromagnetic energy has been investigated numerically. A generalized mathematical model and an effective calculation procedure are proposed. A preliminary case study indicates the successful implementation of the numerical procedure. A two-dimensional microwave melting model is then validated against available experimental results and subsequently used as a tool for efficient computational prototyping. Simulation results are in good agreement with available experimental results. The successful comparison with experiments should give confidence in the proposed mathematical treatment, and encourage the acceptance of this method as useful tool for exploring practical problems. Furthermore, for microwave melting, in case of installed resonator strongly affects on of temperature and microwave power absorbed distribution, and melting front rate, because the microwave can transmit through the sample and then reflect from resonator back in the sample, forming a standing wave within the sample.

The next step, which has already begun, is to couple the grid generation algorithm with the complete transport equations that determine the moving boundary front and buoyancy-driven convection in the liquid. The influence of adjusted meshes number in each layer on thermal flow solution will be investigated. Moreover, some experimental studies will be performed to completely validate numerical results.

Acknowledgments

The authors gratefully acknowledge the Thailand Research Fund (TRF) for supporting this research project.

References

[1] B.J. Pangrle, K.G. Ayappa, H.T. Davis, E.A. Davis, J. Gordon, Microwave thawing of cylinders, Am. Inst. Chem. Eng. 37 (1991) 1789–1800.
[2] B.J. Pangrle, K.G. Ayappa, E. Sutanto, H.T. Davis, E.A. Davis, Microwave thawing of semi-infinite slabs, Chem. Eng. Commun. 112 (1991) 39.
[3] P. Rattanadecho, Theoretical and experimental investigation of microwave thawing of frozen layer using a microwave oven (effects of layered configurations and layer thickness), Int. J. Heat Mass Transfer 47 (2004) 937–945.
[4] A.C. Cleland, R.L. Earl, Assessment of freezing time prediction methods, J. Food Sci. 49 (1984) 1034–1042.
[5] P. Taoukis, E.A. Davis, H.T. Davis, J. Gordon, Y. Talmon, Mathematical modeling of microwave thawing by modified isotherm migration method, J. Food Sci. 52 (1994) 455–463.
[6] X. Zeng, A. Faghri, Experimental and numerical study of microwave thawing heat transfer for food materials, ASME J. Heat Transfer 116 (1994) 446–455.
[7] T. Basak, K.G. Ayappa, Analysis of microwave thawing of slab with the effective heat capacity method, Am. Inst. Chem. Eng. 43 (1997) 1662–1674.
[8] P. Rattanadecho, The simulation of microwave heating of wood using a rectangular waveguide: influence of frequency and sample size, Chem. Eng. Sci. 61 (14) (2006) 4798–4811.
[9] P. Rattanadecho, W. Klinbun, Theoretical analysis of microwave heating of dielectric materials filled in a rectangular waveguide with various resonator distances, ASME J. Heat Transfer 133 (2011), doi:10.1115/1.4002628.
[10] P. Rattanadecho, K. Aoki, M. Akahori, The characteristics of microwave melting of frozen packed beds using a rectangular waveguide, IEEE Trans. Microwave Theory Tech. 50 (6) (2002).
[11] K. Charn-Jung, M. Kaviany, Numerical method for phase-change problems with convection and diffusion, Int. J. Heat Mass Transfer 35 (1992) 457–467.
[12] S. Chellaiah, R. Viskanta, Freezing of saturated and superheated liquid in porous media, Int. J. Heat Mass Transfer 31 (1988) 321–330.
[13] A.B. Crowley, Numerical solution of Stefan problems, Int. J. Heat Mass Transfer 21 (1978) 215.
[14] N. Shamsundar, E.M. Sparrow, Effect of density change on multi-dimensional conduction phase change, ASME J. Heat Transfer 105 (1976) 550.
[15] J. Crank, R.S. Gupta, Isotherm migration method in two dimensions, Int. J. Heat Mass Transfer 18 (1975) 1101.
[16] F.B. Cheung, T.C. Chawla, D.R. Pedersen, The effect of heat generation and wall interaction on freezing and melting in finite slab, Int. J. Heat Mass Transfer 27 (1984) 29.
[17] A. Chatterjee, V. Prasad, A full three-dimensional adaptive finite volume scheme for transport and phase-change process, Part I: formulation and validation, Numer. Heat Transfer A: Appl. 37 (2000) 801–821.
[18] Z.X. Gong, A.S. Mujumdar, Flow and heat transfer in convention-dominated melting in rectangular cavity heated from below, Int. J. Heat Mass Transfer 41 (1998) 2573–2580.
[19] L.E. Eriksson, Generation of boundary-conforming grid around wing-body configurations using transfinite interpolation, AIAA J. 20 (1982) 1313–1320.

[20] W.A. Cook, Body oriented coordinates for generating 3-dimentional meshes, Int. J. Numer. Methods Eng. (1974) 27–43.
[21] W.J. Gordon, C.A. Hall, Construction of curvilinear coordinate systems and applications to mesh generation, Int. J. Numer. Methods Eng. 7 (1973) 461–477.
[22] H.M. Ettouney, R.A. Brown, Finite-element methods for steady solidification problems, J. Comput. Phys. 49 (1983) 118–150.
[23] P. Rattanadecho, Simulation of melting of ice in a porous media under multiple constant temperature heat sources using a combined transfinite interpolation and PDE methods, Chem. Eng. Sci. 61 (2006) 4571–4581.
[24] P. Rattanadecho, S. Wongwises, Moving boundary-moving mesh analysis of freezing process in water-saturated porous media using a combined transfinite interpolation and PDE mapping methods, ASME J. Heat Transfer 31 (2007) 318–333.
[25] P. Ratanadecho, K. Aoki, M. Akahori, A numerical and experimental investigation of the modeling of microwave heating for liquid layers using a rectangular waveguide (effects of natural convection and dielectric properties), Appl. Math. Model. 26 (3) (2002) 449–472.
[26] G. Mur, Absorbing boundary conditions for the finite-difference approximation of the time-domain electromagnetic-field equations, IEEE Trans. Electromagn. Compat. EMC-23 (4) (1981) 377–382.
[27] J.D. Anderson, Computational Fluid Dynamics, International Editions., McGraw-Hill, New York, 1995. Chapter 5.
[28] K.S. Yee, Numerical solution of initial boundary value problems involving Maxwell's equation in isotropic media, IEEE Trans. Antennas Propag. AP-14 (1966) 302–307.